Double-differential cross section for ionization of H_2O molecules by 4-MeV/u C^{6+} and Si^{13+} ions

Shamik Bhattacharjee,[1] S. Biswas,[1] J. M. Monti,[2] R. D. Rivarola,[2] and L. C. Tribedi[1,*]
[1]*Tata Institute of Fundamental Research, Homi Bhabha Road, Coloba, Mumbai 400005, India*
[2]*Instituto de Fisica Rosario (CONICET-UNR), Universidad Nacional de Rosario, 2000 Rosario, Argentina*
(Received 31 January 2017; revised manuscript received 14 July 2017; published 27 November 2017)

Double-differential cross section (DDCS) for electrons ejected in collisions of fast C^{6+} and Si^{13+} projectiles, with a H_2O vapor target, were measured. The electrons were detected over an energy range of 1–600 eV and an angular range of 20°–160°. The obtained DDCS spectra, for both the ions, were compared with the CDW-EIS model. Occasional reference has been made to the DDCS data for the case of 3.75-MeV/u O^{8+} colliding on the same molecule for an overall comparison. A reasonable agreement with theoretical results was seen for the case of C^{6+} and O^{8+} projectiles. However, between C^{6+} and O^{8+} projectiles, the deviation from theory is larger for the case of the carbon projectile. Substantial deviation starts to show up for the case of the Si^{13+} projectile. By numerical integration of the DDCS data, the single-differential cross section (SDCS) and total cross section (TCS) were obtained and compared with theoretical models. The present TCS data along with the other available data for p, He, and C ions were plotted together. A clear and gradual deviation from the Bethe-Born predicted q^2 scaling was observed, where q is the projectile charge state. From all the data we find TCS varies as q^n where $n = 1.7 \pm 0.1$. The provided data set will be valuable in order to help model the radiation damage in hadron therapy, particularly in the Bragg peak region.

DOI: 10.1103/PhysRevA.96.052707

I. INTRODUCTION

In a collision between high-velocity ions with neutral atoms or molecules, a portion of the energy is transferred for the ionization process, i.e., in the ejection of electrons from the target. The study of ionization is very important in various fields like upper atmospheric physics, radiation damage studies, etc. Radiation therapy using proton and highly charged ion beams is quite common. Interaction of high-velocity ions with biological tissues produces a large number of secondary electrons. These secondary electrons can initiate further ionization and excitation processes which may lead to single- and double-strand breaks of the DNA molecule [1]. Therefore it is very important to exactly determine the energy distribution of these secondary electrons for the simulation of radiation damage. It thus becomes very important to obtain an accurate description of total and differential cross sections for ionization of the water molecule induced by highly charged ions, since water constitutes on average about 60% of a human body weight. Energy deposition by heavy ions increases with penetration depth up to the sharp maximum at the end of their range, known as the Bragg peak region. Proton therapy is the most widely used technique for treating cancer cells. However, radiation therapy using heavier beams like carbon is also quite common [2]. Carbon ion beams allow a highly localized deposition of energy that can be utilized for increasing radiation doses to cancer cells while minimizing irradiation to adjacent normal tissues. The lateral fall-off of the radiation beam around the target is steeper with the carbon ion beam than for the proton beam. Many laboratories are being set up which are dedicated for radiation therapy using the carbon ion beam. Therefore, it is important to understand the heavy ion collisions with water molecules in order to help model the radiation therapy for biological matter.

On the experimental side several experiments have been carried out to study ionization of biological molecules bombarded with high-velocity ions [3–10]. A good number of results are available in the literature on total cross sections for ionization and/or dissociation of water molecules under the impact of charged projectiles, such as e^- [11,12], H^+ [13–17], He^{q+} [14,15], Ne^{q+} [18–20], and other heavier ions like C^{3+} and O^{5+} [21]. But when it comes to the measurement of differential cross sections, the literature is not so vast and most of the existing results are for light projectiles like e^- [22], H^+ [23,24], or $He^{1+,2+}$ [25], He^{2+}[26]. Differential cross section measurements for highly charged projectiles are rare. Among the few results reported for projectiles heavier than helium are carbon ion data of Ohsawa *et al.* [27,28] and bare carbon and oxygen ion data [29,30] (see also Ohsawa *et al.* [31]).

In the present paper we report the measurement of the double-differential, single-differential, and total cross sections for ionization of water molecules under the impact of 4-MeV/u C^{6+} and Si^{13+} ions. In addition similar data for nearly the same velocity O ions are also used for comprehensive study. The same velocity but different charge state (q) of the ions enables us to inspect projectile q dependence on the total cross section. Also, ionization by projectiles like Si^{13+} can test the comparison between theoretical calculations and experimental results for such highly charged projectiles. However, for the purpose of a comprehensive discussion on the projectile energy dependence, a new set of data for 3.75-MeV/u O^{8+} on H_2O is also used occasionally. The experimental data have been compared with both the prior and post-versions of the continuum distorted wave–eikonal initial state (CDW-EIS) model [32,33].

II. THEORY

From the theoretical point of view, the simplest model for the ionization process involves a three-particle system interacting through long-range Coulomb potentials. The

*lokesh@tifr.res.in; ltribedi@gmail.com

theoretical calculations based on the distorted wave approximation have been used for many years. The continuum distorted wave–eikonal initial state (CDW-EIS) approximation [34,35] has probably been one of the most widely employed model for studying ion-atom ionization. In this work, a particular approach is considered within the CDW-EIS model in order to describe the initial molecular orbitals, namely the complete neglect of differential orbitals (CNDO) one, where each one of them in the initial channel is written as a linear combination of orbitals of the atomic constituents of the molecule [36,37]. The molecular orbitals are described using a Roothaan-Hartree-Fock approximation of the atomic compounds of the molecular orbital [38], so that radial correlation is included in each one of the corresponding atomic states. Details of the model are given in [33]. In this theory, single ionization is described by an independent-electron approximation assuming that the nonionized electrons remain frozen during the collision process. The Coulombic behavior due to the active electron-projectile interaction is included in the entry channel by choosing a distorted initial wave function where the initial bound state Φ_i is multiplied by an eikonal phase $\mathcal{L}_i^+$, associated with that interaction:

$$\chi_i^+ = \Phi_i \, \mathcal{L}_i^+. \tag{1}$$

In the exit channel, the active electron is assumed to feel simultaneously the fields of the projectile and of the residual target. So, the final wave function is composed as a product of the continuum target wave function Φ_f, and a projectile continuum factor $\mathcal{L}_f^-$:

$$\chi_f^- = \Phi_f \, \mathcal{L}_f^-. \tag{2}$$

The *prior* version of the transition amplitude for the CDW-EIS approximation can be written as

$$\mathcal{A}_{if}^- = -i \int_{-\infty}^{+\infty} dt \, \langle \chi_f^- | (W_i | \chi_i^+ \rangle), \tag{3}$$

provided now that the initial distorted wave function χ_i^+ does not contribute to the transition amplitude as $t \to +\infty$.

In (3), W_i is the well-known EIS perturbative operator,

$$W_i \, \chi_i^+ = \left[\tfrac{1}{2} \Phi_i \nabla^2 \mathcal{L}_i^+ + \nabla \Phi_i \cdot \nabla \mathcal{L}_i^+ \right], \tag{4}$$

while the *post*-version of the transition amplitude can be written as

$$\mathcal{A}_{if}^+ = -i \int_{-\infty}^{+\infty} dt \, [\langle \chi_f^- | W_f^\dagger] | \chi_i^+ \rangle, \tag{5}$$

provided that the final distorted wave function χ_f^- does not contribute to the transition amplitude as $t \to -\infty$.

In (5) W_f is the widely used CDW perturbative operator,

$$W_f^- \chi_f^- = [\nabla \Phi_f \cdot \nabla \mathcal{L}_f^-]. \tag{6}$$

This *post*-version is obtained by assuming that the potential that defines the interaction between the ionized active electron and the residual target is a pure Coulomb one generated by an effective charge chosen with some physical criteria. In this approximation a part of the interaction between the ionized electron and the residual target (dynamic screening), composed by the target nucleus and the passive electrons, is neglected and therefore post-prior discrepancies are found since in the *prior* version the radial correlation between the active electron and the passive ones (those that remain bound to the target) is contained via the initial target bound orbitals. As a consequence, if the same initial and final target wave functions are used, the *prior* version appears to be more complete than the *post* one. It has been shown that the use of more elaborated Moccia functions [39] to describe the initial molecular orbitals in the calculation of double-differential cross sections (averaged over all molecular orientations) gives results that are in close agreement to those obtained within the CNDO approximation [33], in both *prior* and *post* versions, of double-differential cross sections averaged over all molecular orientations. This justifies the use of the CNDO approximation to calculate the double-differential cross sections. Thus, from the formal point of view, the *prior* version contains a more complete physical information.

III. MEASUREMENT TECHNIQUES

For the present work, 4-MeV/u C^{6+} and Si^{13+} ion beams were provided by the BARC-TIFR Pelletron accelerator facility in T.I.F.R. Mumbai, India. Figure 1 shows a schematic diagram of the experimental setup. Before entering the experimental chamber, the beam was properly collimated by using two four-jaw slit assemblies separated 1 m apart. Another aperture of 4 mm radius was used just before the interaction chamber. A base pressure of 3×10^{-7} mbar was maintained inside the chamber. This kind of high vacuum was obtained using a turbo molecular pump with pumping speed of 2000 l/s backed by a tri-scroll dry pump. The inner side of the scattering chamber was covered with two sets of thin μ-metal sheets to reduce the earth's magnetic field inside the chamber to a value of 7–10 mG. This was essential for detecting low energy electrons (<10 eV). The number of electrons (N_e) with the proper energy and direction was counted by using a channel electron multiplier (CEM). Prior to entering the CEM, the electrons were energy analyzed by an electrostatic hemispherical analyzer. The inner and outer radius of the electrodes are 2.5 cm and 3.5 cm, respectively. The angles of deflection were chosen as 20°, 30°, 40°, 50°, 60°, 70°, 80°, 90°, 105°, 120°, 135°, 150°, and 160° and the range of electron energies was 1–600 eV. A container containing about 100 ml of deionized water was connected with the gas inlet port of the chamber. The experiment was performed in a uniform-gas-density condition which allowed the measurement of absolute cross sections. The vapor pressure of water at room temperature is about 27 Torr. As the pressure inside the chamber is sufficiently low, water vapor automatically flows inside the chamber. This flow was controlled by a solenoid valve connected between the water container and the chamber. During the experiment, the entire chamber was flooded with water vapor at a pressure of about 0.15 mTorr. This pressure was measured using a MKS baratron capacitance manometer. During the experiment, the cylindrical surface of the chamber was heated and kept at a temperature of about 40°C. The temperature at the center of the chamber was measured to be 34°C, which was higher than the room temperature only by about 7°C causing the gas density reduction only by a few percent which is included in the total error estimation. The wall heating reduced the sticking of water molecules on the

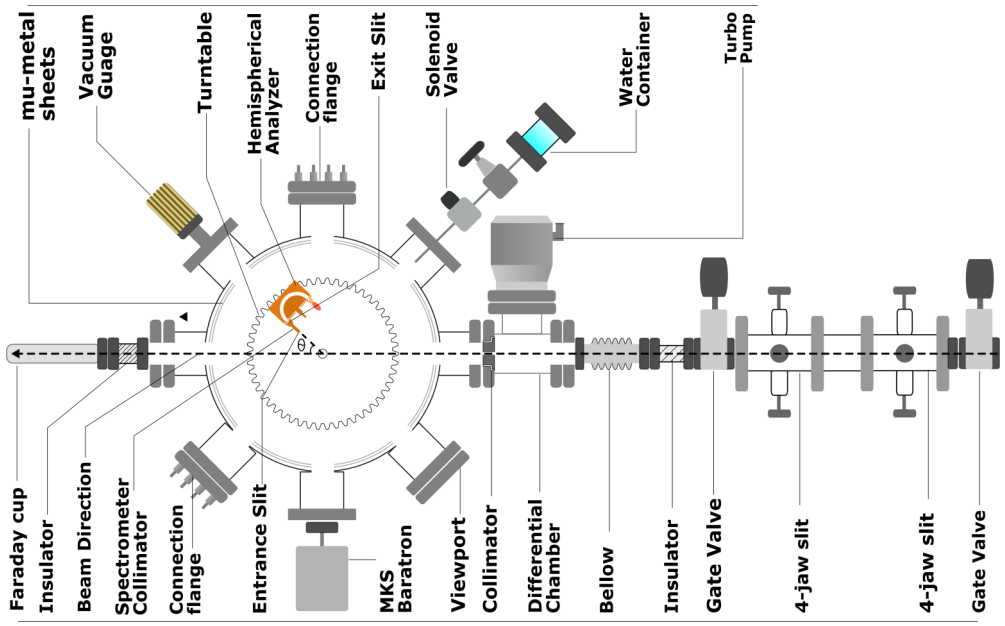

FIG. 1. A schematic diagram of the experimental setup.

chamber wall and hence reduced the background to about 2%–5% of the data, below 100 eV, and maximum to about 10%–12% at higher energies. Good statistics was maintained during the experiment. So the statistical error was less than 5% for most of the angles and most of the energies. However, in some cases, i.e., for large backward angles and higher energy electrons (above 200 eV) this could be maximum 10%–12%. The overall error arises due to the uncertainty in the measurement of water-vapor density n (±7%–10%), spectrometer resolution (±10%), efficiency (±5%–6%), and the solid angle path length integral (±8%–10%). The absolute error was estimated to be ≈18%–20%. If the number density of the gas inside the chamber is n and for N_p number of projectiles, N_e number of secondary electrons having energy ϵ and solid angle path length $(l\Omega)_{\rm eff}$ were detected, then the DDCS values were calculated using the following equation:

$$\frac{d^2\sigma}{d\Omega_e d\epsilon} = \frac{N_e}{N_p n \epsilon_{\rm el} (l\Omega)_{\rm eff} \Delta\epsilon}. \tag{7}$$

The quantity $\Delta\epsilon$ is the energy resolution of the spectrometer, which was measured to be 6% of the electron energy, i.e., $\Delta\epsilon = 0.06(e + V_c)$, in which V_c is the pre-acceleration voltage (6 V). This voltage was applied to the entrance and exit slits of the analyzer to increase the efficiency of detection of low energy electrons. The detection efficiency of the CEM ($\epsilon_{\rm el}$), is taken to be 0.9 as mentioned in the operation manual of the CEM used. The solid angle path length is given by $(l\Omega)_{\rm eff} = \frac{w_1 w_2 h_2}{LR\sin\theta}$ [40], where θ is the electron emission angle with respect to the beam direction. Here, w_1 is the width for the entrance slit, and w_2 and h_2 are, respectively, the width and height of the exit slit of the spectrometer collimator. The length of the spectrometer collimator is given by L, and R is the distance of the entrance slit from the center of the interaction zone. Density of H_2O molecules inside the chamber was calculated from the measured pressure. Pressure inside the chamber was kept sufficiently low (≈1×10^{-4} Torr) so as to ensure a single collision condition by projectile ions. During the experiment the typical beam current was about 50 nA.

IV. EXPERIMENTAL RESULTS

A. Double-differential cross sections

1. Energy distribution

Figures 2 and 3 show three-dimensional plots, representing the measured energy dependence of the DDCS for all the angles in the case of 48-MeV C^{6+} and 112-MeV Si^{13+} projectiles, respectively. Detailed analysis of the DDCS plots and its comparison with theoretical models are shown in Figs. 4 and 5. The measured absolute DDCS values for both C^{6+} and Si^{13+} projectiles are tabulated in Tables I and II, respectively. In Figs. 4(a) and 4(b), and 5(a) and 5(b), the DDCS values are plotted as a function of emitted electron energy for fixed values of θ. Though a total of 13 different angles have been studied, only six are shown here for better clarity. The DDCS spectrum falls off rapidly as electron energy increases and at

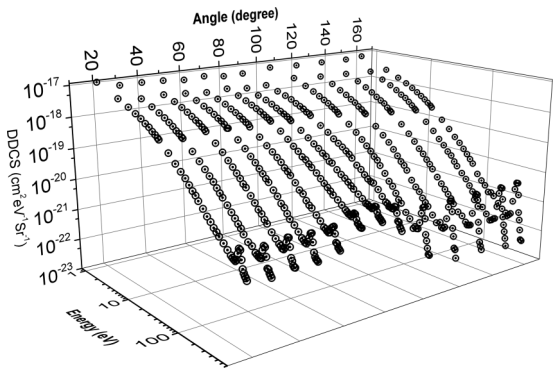

FIG. 2. 3D plot showing DDCS energy distribution measured at all the angles for the 48-MeV C^{6+} projectile.

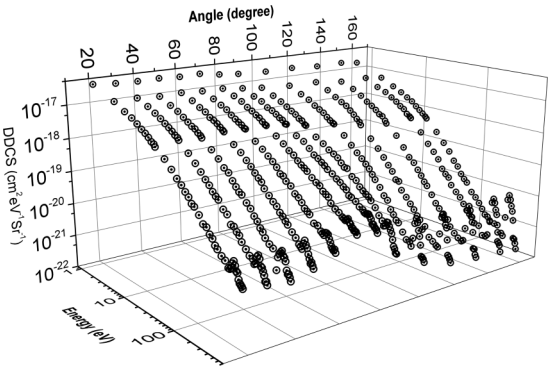

FIG. 3. Same as in Fig. 2 but for the 112-MeV Si^{13+} projectile.

the highest energy (∼600 eV) it is 4–5 orders of magnitude smaller than its value at lowest energy (∼1 eV). In all the plots the experimental results are compared with both the prior and post-versions of the CDW-EIS model. The electron spectra reveal different regions which can be associated with specific electron production mechanisms. Lowest energy electrons are emitted in soft collision (SC) processes, which are characterized by small energy and momentum transfers involving small projectile deflections. After that, in the intermediate energy region, the two-center effect influences the spectrum. The two-center effect becomes important since the outgoing electron is influenced by the superposition of the fields of the residual target and the projectile nucleus. The projectile attracts the electron producing thus an enhancement of electron emission in the forward direction. The sharp peak near 480 eV on all the curves corresponds to the K-LL Auger electron emission from the target oxygen atom.

Figures 4(a) and 4(b) show the energy distributions for the C^{6+} projectile. The plots show a reasonably good agreement with theoretically calculated DDCS values. The agreement with the prior version of the CDW-EIS model [represented by the solid(red) line] goes better as the electron energy

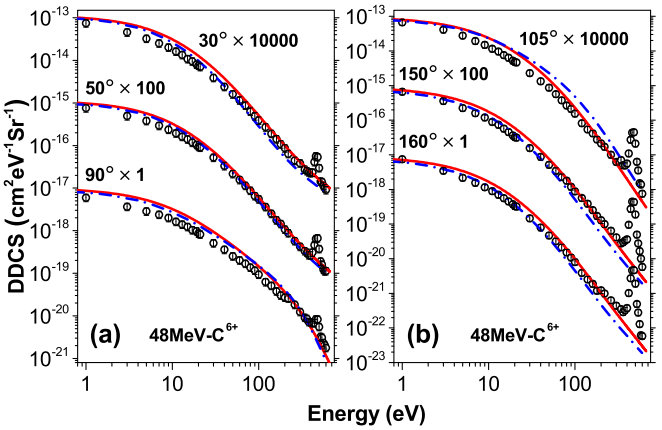

FIG. 4. The absolute electron DDCS for six different emission angles for the 48-MeV C^{6+} projectile. In each plot, the solid(red) line corresponds to the prior version of the CDW-EIS model calculations and the dash-dotted(blue) line corresponds to its post-version. For convenience, data and theory have been multiplied by suitable factors as indicated in the figure.

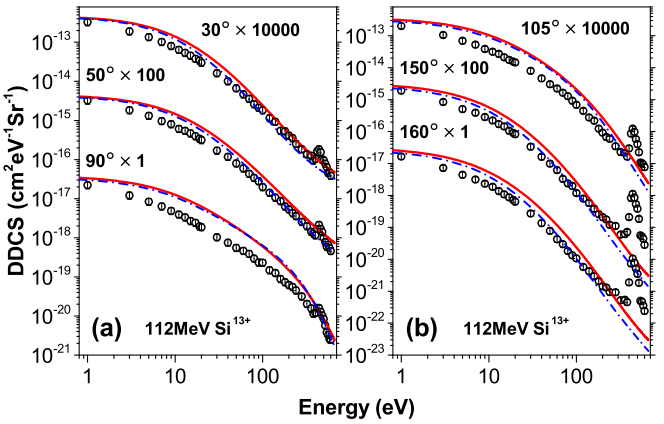

FIG. 5. Same as in Fig. 4 but for 112-MeV Si^{13+} ions.

increases. This could be attributed to the fact that for higher energy electron emission closer collisions contribute to the reaction, and so the dynamic screening (the interaction with the passive electrons) must be considered. However, for even higher emission energies (not shown here) this interaction should play a minor role. In the lower energy region, theory overestimates the experimental results, for almost all angles. However, the deviation is slightly larger for angles between 75° and 105° (see below for detail). The post version of the CDW-EIS model [represented by the dash-dotted(blue) line] exhibits a similar kind of behavior. In general it also matches remarkably well with the experimental data for almost all the emission angles.

Figures 5(a) and 5(b) show the DDCS plots for the Si^{13+} projectile along with the CDW-EIS prior [solid (red) line] and post-[dash-dotted(blue) line] model calculation. It is clear from the plots that the deviation of the theoretical model from experimental results is larger for the case of the Si^{13+} projectile than for the C^{6+} projectile. The origin of this behavior could be related to the higher perturbation strength caused by the Si projectile (see below) and may be a matter of further research. Deviation is less for extreme forward and extreme backward angles. The post- and prior models almost matches for 50°, 90°, and 105° for both the projectiles (see Figs. 5 and 4). Interestingly the post-version works better for extreme forward (30°) and backward angles (160°) The deviation is again large for angles between 50° and 105° as was seen in the case of the C^{6+} projectile. This behavior cannot be understood fully at this stage.

Figure 6 shows the ratio of data to theoretical DDCS values for C^{6+} and Si^{13+} projectiles. We have also added the data of O^{8+}. The velocity of the O^{8+} projectile is nearly close (3.75 MeV/u) to that for the C and Si ions. It is clear from the plots that out of the three projectiles, the Si^{13+} projectile shows the highest deviation from the theoretical predictions. For the Si^{13+} projectile in some energy region, theory overestimates experimental data by 3–3.5 times. The C^{6+} also shows a good agreement with theoretical predictions, however, better agreement is seen in the case of the O^{8+} projectile. The agreement could be expected to be better in the case of C^{6+} since the net projectile charge is lower than that corresponding to O^{8+}. The perturbation strength (s) for 4-MeV/u C^{6+} is smaller than that for O^{8+}. However, this

TABLE I. DDCS ($cm^2eV^{-1}Sr^{-1}$), SDCS(θ) (cm^2Sr^{-1}), SDCS(ϵ)(cm^2eV^{-1}), and TCS (cm^2) for the case of the C^{6+} projectile. Numbers in brackets indicate power of 10.

E (eV)	30°	40°	50°	60°	70°	80°	90°	105°	120°	135°	150°	$\frac{d\sigma}{d\epsilon}$
1	7.48[−18]	7.59[−18]	7.23[−18]	6.29[−18]	6.92[−18]	5.78[−18]	5.95[−18]	7.37[−18]	6.78[−18]	6.77[−18]	6.73[−18]	8.05[−17]
5	3.27[−18]	3.81[−18]	3.34[−18]	2.99[−18]	3.12[−18]	2.57[−18]	2.87[−18]	3.22[−18]	2.80[−18]	2.61[−18]	2.26[−18]	3.50[−17]
9	2.02[−18]	2.38[−18]	2.16[−18]	1.90[−18]	2.03[−18]	1.74[−18]	2.00[−18]	1.87[−18]	1.51[−18]	1.36[−18]	1.20[−18]	2.13[−17]
13	1.35[−18]	1.62[−18]	1.48[−18]	1.36[−18]	1.49[−18]	1.22[−18]	1.41[−18]	1.28[−18]	9.67[−19]	8.40[−19]	7.44[−19]	1.45[−17]
17	9.56[−19]	1.18[−18]	1.11[−18]	9.99[−19]	1.12[−18]	9.42[−19]	1.04[−18]	8.99[−19]	6.45[−19]	5.31[−19]	4.58[−19]	1.04[−17]
20	7.54[−19]	9.37[−19]	9.10[−19]	7.78[−19]	9.25[−19]	7.51[−19]	8.67[−19]	6.79[−19]	4.87[−19]	4.00[−19]	3.29[−19]	8.18[−18]
40	2.40[−19]	3.34[−19]	3.25[−19]	3.04[−19]	3.66[−19]	3.13[−19]	3.60[−19]	2.45[−19]	1.35[−19]	1.03[−19]	8.81[−20]	2.94[−18]
60	1.16[−19]	1.57[−19]	1.58[−19]	1.69[−19]	1.96[−19]	1.82[−19]	2.03[−19]	1.12[−19]	5.69[−20]	3.98[−20]	3.49[−20]	1.49[−18]
80	6.38[−20]	8.77[−20]	8.86[−20]	9.82[−20]	1.29[−19]	1.22[−19]	1.38[−19]	5.98[−20]	2.68[−20]	2.00[−20]	1.81[−20]	8.87[−19]
100	3.93[−20]	5.54[−20]	5.72[−20]	6.72[−20]	8.60[−20]	8.75[−20]	9.32[−20]	3.50[−20]	1.56[−20]	1.10[−20]	8.87[−21]	5.77[−19]
140	1.91[−20]	2.52[−20]	2.79[−20]	3.08[−20]	4.88[−20]	4.82[−20]	5.11[−20]	1.36[−20]	5.49[−21]	4.34[−21]	3.91[−21]	2.86[−19]
180	1.08[−20]	1.46[−20]	1.55[−20]	1.78[−20]	3.16[−20]	3.34[−20]	3.04[−20]	6.65[−21]	2.80[−21]	2.29[−21]	1.72[−21]	1.69[−19]
220	6.40[−21]	8.84[−21]	8.31[−21]	1.23[−20]	2.16[−20]	2.34[−20]	2.58[−20]	3.65[−21]	1.71[−21]	1.23[−21]	1.00[−21]	1.19[−19]
260	4.45[−21]	5.76[−21]	6.38[−21]	8.67[−21]	1.74[−20]	1.84[−20]	1.84[−20]	2.10[−21]	1.01[−21]	7.53[−22]	6.44[−22]	8.61[−20]
300	3.85[−21]	4.24[−21]	4.54[−21]	6.49[−21]	1.35[−20]	1.49[−20]	1.24[−20]	1.47[−21]	6.28[−22]	6.14[−22]	4.18[−22]	6.32[−20]
340	2.76[−21]	3.33[−21]	3.31[−21]	4.68[−21]	1.07[−20]	1.17[−20]	9.11[−21]	7.94[−22]	7.08[−22]	4.21[−22]	2.78[−22]	4.74[−20]
360	2.55[−21]	3.09[−21]	3.03[−21]	4.41[−21]	9.69[−21]	1.15[−20]	8.57[−21]	9.46[−22]	5.04[−22]	3.48[−22]	2.98[−22]	4.47[−20]
380	2.37[−21]	2.68[−21]	2.67[−21]	3.93[−21]	8.74[−21]	1.04[−20]	7.22[−21]	8.53[−22]	4.95[−22]	3.60[−22]	3.38[−22]	3.96[−20]
420	2.33[−21]	3.10[−21]	3.08[−21]	3.85[−21]	8.01[−21]	9.57[−21]	6.80[−21]	1.43[−21]	1.11[−21]	9.63[−22]	9.58[−22]	4.14[−20]
460	5.63[−21]	6.49[−21]	5.75[−21]	6.02[−21]	1.06[−20]	1.20[−20]	8.35[−21]	4.56[−21]	4.39[−21]	4.45[−21]	4.46[−21]	7.47[−20]
480	5.37[−21]	6.67[−21]	6.07[−21]	6.45[−21]	1.03[−20]	1.20[−20]	8.28[−21]	4.89[−21]	4.54[−21]	4.34[−21]	4.36[−21]	7.56[−20]
520	1.45[−21]	1.90[−21]	1.81[−21]	2.32[−21]	5.87[−21]	6.79[−21]	3.24[−21]	7.07[−22]	6.37[−22]	5.71[−22]	4.99[−22]	2.48[−20]
560	1.14[−21]	1.23[−21]	1.22[−21]	1.76[−21]	4.93[−21]	5.78[−21]	2.33[−21]	2.76[−22]	1.52[−22]	1.32[−22]	1.67[−22]	1.77[−20]
600	9.12[−22]	1.14[−21]	1.10[−21]	1.51[−21]	4.74[−21]	4.85[−21]	1.78[−21]	1.75[−22]	7.57[−23]	7.80[−23]	5.83[−23]	1.49[−20]
$\frac{d\sigma}{d\Omega}$	6.22[−17]	7.43[−17]	6.9[−17]	6.5[−17]	7.53[−17]	6.6[−17]	7.14[−17]	5.98[−17]	4.54[−17]	4.08[−17]	3.66[−17]	7.22[−16](TCS)

TABLE II. Same as in Table I, but for the Si^{13+} projectile. Numbers in brackets indicate power of 10.

E (eV)	30°	40°	50°	60°	70°	80°	90°	105°	120°	135°	150°	$\frac{d\sigma}{d\epsilon}$
1	3.29[−17]	3.18[−17]	3.27[−17]	3.04[−17]	3.17[−17]	2.54[−17]	2.23[−17]	2.05[−17]	2.10[−17]	1.87[−17]	1.93[−17]	2.95[−16]
5	1.37[−17]	1.19[−17]	1.33[−17]	1.23[−17]	1.24[−17]	9.82[−18]	8.45[−18]	7.02[−18]	7.06[−18]	5.81[−18]	5.08[−18]	1.08[−16]
9	8.08[−18]	7.08[−18]	8.10[−18]	7.58[−18]	7.25[−18]	5.77[−18]	4.92[−18]	3.92[−18]	3.71[−18]	2.81[−18]	2.87[−18]	6.24[−17]
13	5.42[−18]	4.66[−18]	5.46[−18]	4.78[−18]	5.07[−18]	4.26[−18]	3.36[−18]	2.72[−18]	2.33[−18]	1.76[−18]	1.72[−18]	4.18[−17]
17	3.81[−18]	3.47[−18]	3.98[−18]	3.65[−18]	3.64[−18]	3.22[−18]	2.45[−18]	1.78[−18]	1.42[−18]	1.23[−18]	1.06[−18]	2.97[−17]
20	3.01[−18]	2.71[−18]	3.18[−18]	3.01[−18]	3.00[−18]	2.60[−18]	1.88[−18]	1.48[−18]	9.72[−19]	7.73[−19]	8.28[−19]	2.34[−17]
40	1.02[−18]	1.03[−18]	1.18[−18]	1.13[−18]	1.25[−18]	1.14[−18]	7.60[−19]	4.66[−19]	2.48[−19]	1.83[−19]	1.63[−19]	8.53[−18]
60	4.70[−19]	5.37[−19]	5.98[−19]	6.30[−19]	7.37[−19]	5.71[−19]	4.68[−19]	2.24[−19]	9.26[−20]	7.30[−20]	6.25[−20]	4.46[−18]
80	2.63[−19]	2.63[−19]	3.42[−19]	3.34[−19]	4.53[−19]	4.08[−19]	2.97[−19]	1.30[−19]	3.84[−20]	3.32[−20]	2.41[−20]	2.62[−18]
100	1.85[−19]	1.83[−19]	1.99[−19]	2.38[−19]	3.40[−19]	2.89[−19]	2.32[−19]	6.91[−20]	2.05[−20]	1.78[−20]	1.20[−20]	1.80[−18]
140	9.36[−20]	9.63[−20]	1.08[−19]	1.30[−19]	2.01[−19]	1.89[−19]	1.26[−19]	2.78[−20]	9.51[−21]	6.13[−21]	5.86[−21]	1.00[−18]
180	5.32[−20]	5.18[−20]	6.40[−20]	8.76[−20]	1.32[−19]	1.32[−19]	7.33[−20]	1.25[−20]	4.79[−21]	3.13[−21]	2.61[−21]	6.22[−19]
200	4.14[−20]	3.68[−20]	5.40[−20]	6.49[−20]	1.16[−19]	1.15[−19]	6.23[−20]	9.35[−21]	3.82[−21]	2.33[−21]	2.10[−21]	5.17[−19]
240	2.55[−20]	2.26[−20]	3.62[−20]	4.95[−20]	7.35[−20]	7.88[−20]	4.56[−20]	5.98[−21]	2.73[−21]	1.57[−21]	1.21[−21]	3.51[−19]
280	1.86[−20]	1.74[−20]	2.57[−20]	3.14[−20]	5.68[−20]	6.68[−20]	3.18[−20]	3.52[−21]	1.42[−21]	1.10[−21]	1.12[−21]	2.61[−19]
320	1.38[−20]	1.48[−20]	1.99[−20]	3.00[−20]	4.92[−20]	5.13[−20]	2.05[−20]	2.30[−21]	1.16[−21]	8.60[−22]	6.01[−22]	2.07[−19]
380	9.55[−21]	9.79[−21]	1.30[−20]	2.09[−20]	3.77[−20]	3.97[−20]	1.15[−20]	1.65[−21]	8.84[−22]	8.18[−22]	7.22[−22]	1.48[−19]
420	1.64[−20]	1.46[−20]	1.71[−20]	2.35[−20]	3.81[−20]	3.97[−20]	1.61[−20]	8.69[−21]	7.90[−21]	7.69[−21]	8.36[−21]	2.04[−19]
460	1.55[−20]	1.25[−20]	1.69[−20]	2.25[−20]	3.39[−20]	3.45[−20]	1.29[−20]	9.82[−21]	8.11[−21]	8.25[−21]	8.63[−21]	1.90[−19]
480	1.02[−20]	1.16[−20]	1.42[−20]	1.76[−20]	3.10[−20]	3.00[−20]	1.04[−20]	5.88[−21]	5.15[−21]	5.44[−21]	5.38[−21]	1.51[−19]
500	9.66[−21]	9.50[−21]	1.00[−20]	1.44[−20]	2.62[−20]	2.28[−20]	8.43[−21]	4.07[−21]	4.26[−21]	3.76[−21]	3.88[−21]	1.19[−19]
560	4.56[−21]	4.76[−21]	6.62[−21]	9.40[−21]	2.24[−20]	1.86[−20]	3.34[−21]	1.03[−21]	5.98[−22]	5.84[−22]	5.18[−22]	7.27[−20]
600	3.90[−21]	3.20[−21]	4.63[−21]	8.51[−21]	1.85[−20]	1.44[−20]	2.50[−21]	7.77[−22]	4.15[−22]	3.36[−22]	2.85[−22]	5.78[−20]
$\frac{d\sigma}{d\Omega}$	2.59[−16]	2.4[−16]	2.67[−16]	2.58[−16]	2.84[−16]	2.41[−16]	1.83[−16]	1.31[−16]	1.11[−16]	8.99[−17]	8.79[−17]	2.31[−15](TCS)

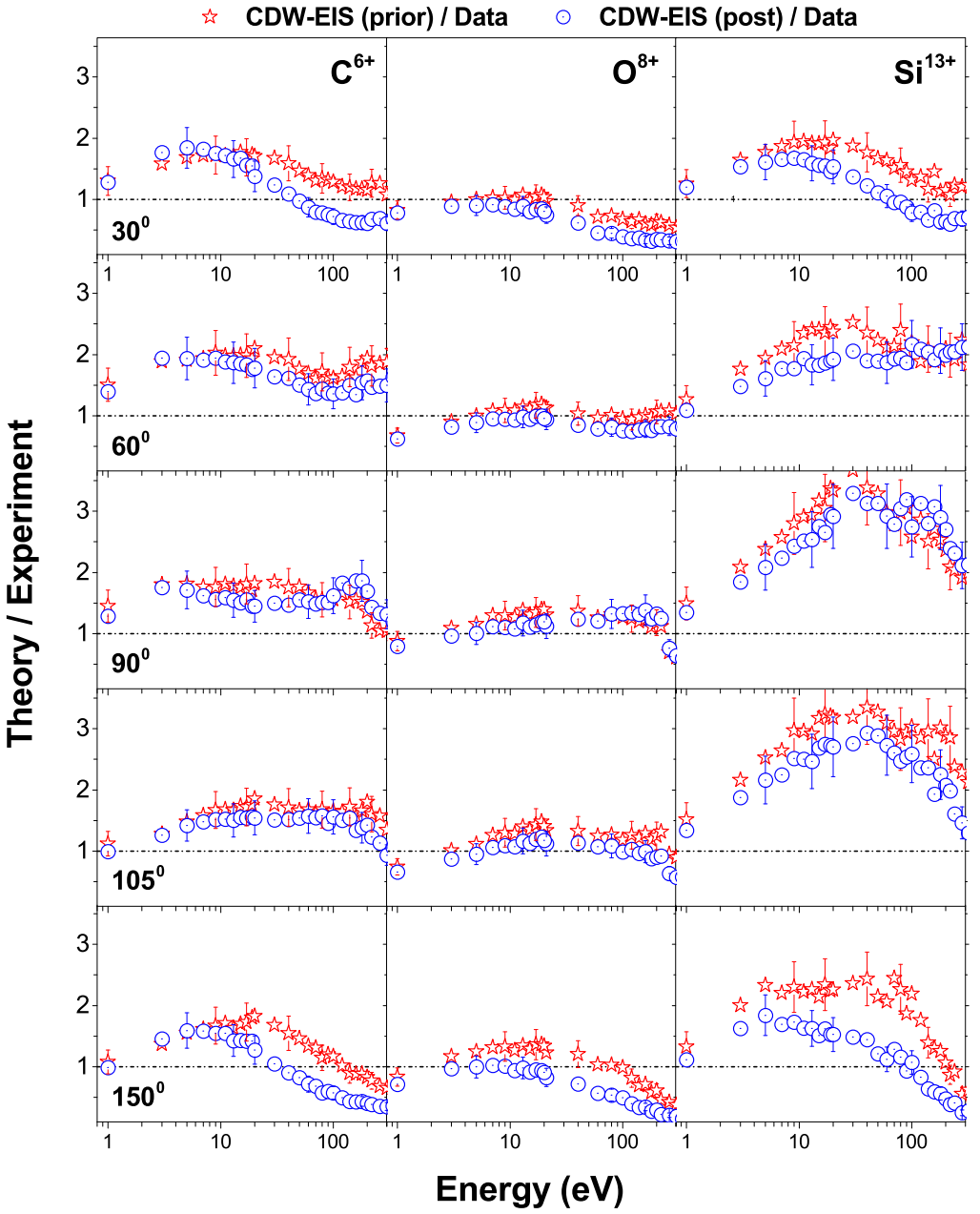

FIG. 6. Ratio of theoretical (CDW-EIS prior and post) and experimental DDCS for C^{6+} (4 MeV/u), O^{8+}(3.75 MeV/u), and Si^{13+} (4 MeV/u) projectiles for five different angles.

consideration, valid for first-order nondistorted wave theories, must be taken with care considering that the projectile-active electron interaction is included in the CDW-EIS calculations through the continuum factors $\mathcal{L}_i^+$ and $\mathcal{L}_f^-$. However, this observation is not fully understood and needs further study.

2. *Angular distribution*

Figures 7 and 8 show the DDCS angular distribution plots for C^{6+} and Si^{13+} projectiles, respectively. For each projectile, we have shown the angular distribution for six different electron energies. The peak at around 80°–90° arises because of the binary nature of collisions. For both the projectiles, a significant difference between theoretical models and experimental results can be seen in this region. This behavior is similar to that previously obtained for 6-MeV/u C^{6+} impact on water molecules [33]. However, for H^+ and He^{2+} projectiles a good theory-experiment agreement was found [33]. It should be noted that the agreement found between CDW-EIS calculations and experimental results for H^+, He^{2+}, and C^{6+} impact on water was very good for lower emission energies [33]. It is in some way in contrast with present results. In case of the Si the deviation of the theory is substantially larger than that for C ions. For the C projectile, the post-version comes closer to the experimental data for extreme forward and backward angles, except for $\epsilon \geqslant 200$ eV (see Fig. 7). For Si ions, the post-version provides a better

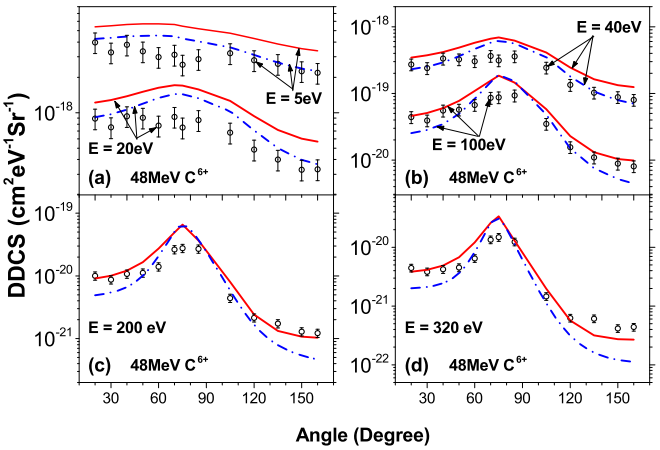

FIG. 7. The angular distributions of the DDCS for different emission energies for the 4-Mev/u C^{6+} projectile. In each plot, the solid(red) line corresponds to the prior version of the CDW-EIS model and the dash-dotted (blue) line corresponds to its post-version.

agreement with the data for most of the angles except between 75° and 105° and except for $\epsilon \geqslant 300$ eV (see Fig. 8).

As electron energy increases this peak becomes more prominent. This can be explained by the fact that, in the low energy region only target field plays the important role, whereas the highest energy electrons are emitted in low impact parameter binary collisions between projectile nucleus and the target active electron which can be considered "nearly free"—since momentum transfer is quite large. As energy of the ejected electron increases the angular distribution shows large asymmetry of DDCS value between forward and backward angles. This kind of forward backward asymmetry is well known and is caused by what is known as the two-Coulomb-center effect [41], where the secondary electrons are influenced by both the moving residual recoil ion and the forward moving projectile ions. This causes a focusing of electrons in the forward direction, and thus giving rise to the asymmetry. This post-collision interaction between the fast moving ion ($v \approx 12.7$ a.u.) and the electron is appreciable for the fast electrons ($\epsilon_e \approx 300$ eV, $v_e \approx 6$ a.u.) emitted in the forward direction compared to slow electrons.

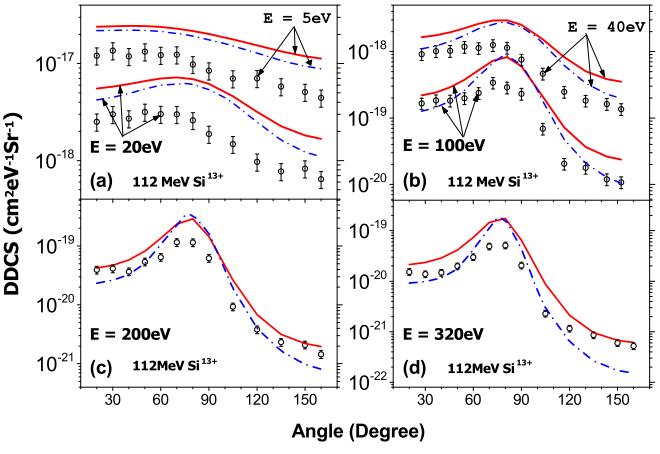

FIG. 8. Same as in Fig. 7 but for the Si^{13+} projectile.

B. Single-differential cross section

As DDCS values were obtained for a wide range of angles and energies it was possible to numerically integrate the data to obtain the single-differential cross section (SDCS), differential in ejection angle $[d\sigma/d\Omega(\theta)]$ or differential in energy $[d\sigma/d\epsilon(\epsilon)]$. In the process of numerical integration, DDCS values for angles 0°–20° and 160°–180° were extrapolated by polynomial fitting technique. This technique gives reasonably accurate values since near the extreme large and small angles the distribution is almost flat or changes very little. The estimated value corresponds to only about 5%–6% of the measured TCS between 20° and 160° The results on the SDCS for both C^{6+} and Si^{13+} beams are shown in the last column of Tables I and II, respectively.

The main contribution to this SDCS comes from directions near 90°, since the peak of the angular distribution lies near this angle due to the binary nature of collision. Therefore a single center ionization model could be expected to give good results with the experimental data. We have compared the SDCS results with both the prior and post-versions of the CDW-EIS model. Figure 9 shows the obtained $d\sigma/d\epsilon$ spectrum as a function of emitted electron energy. For the C^{6+} beam both the theoretical models overestimate the experimental data only slightly [see Fig. 9(a)], especially for the low-energy region. The match gets better for higher electron energies. The differences between the post- and prior CDW-EIS versions could be attributed to the importance of the correlation between the active and passive electrons. Figure 9(c) shows SDCS for the Si^{13+} beam. It also shows a similar type of behavior except that the overestimation of data by the model used is larger. Figure 9(b) shows the SDCS and its comparison with the CDW-EIS model for the 3.75-MeV/u O^{8+} projectile. By comparing Figs. 9(a) and 9(c) with Fig. 9(b), it is clear that oxygen projectile gives the best match with the theoretical models. In Figs. 9(d)–9(f), we have shown the comparison of both the CDW-EIS model calculations with the obtained SDCS in the form of experiment-to-theory ratios. For both the projectiles, the ratio falls outside of absolute error bars. Maximum deviation can be seen for electron energies of about 50 eV. Figure 10 shows the obtained SDCS spectrum as a function of emitted electron angle. Comparison with theory shows our data fall below both the theoretical results for all the angles. For the case of the C^{6+} beam, the prior and post-versions lie outside the error bars of the experimental data [see Fig. 10(a)]. Figure 10(b) represents $d\sigma/d\Omega$ for the Si^{13+} projectile. In this case the overestimation of the theoretical model (prior and post) is much larger than that for the case of the C^{6+} projectile.

C. Total cross sections

Total cross sections (TCS) were obtained by integrating the SDCS values over the emission angle or the emitted electron energies. The integration is done for the entire angular range, from 0° to 180°. As data are not available below 20° and above 160°, those values have been extrapolated. The absolute possible error in estimating the TCS values is about 18%. The TCS results for both C^{6+} and Si^{13+} projectiles along with O^{8+} projectiles are shown in Table III, where the data are compared with different models. It can be seen from the table,

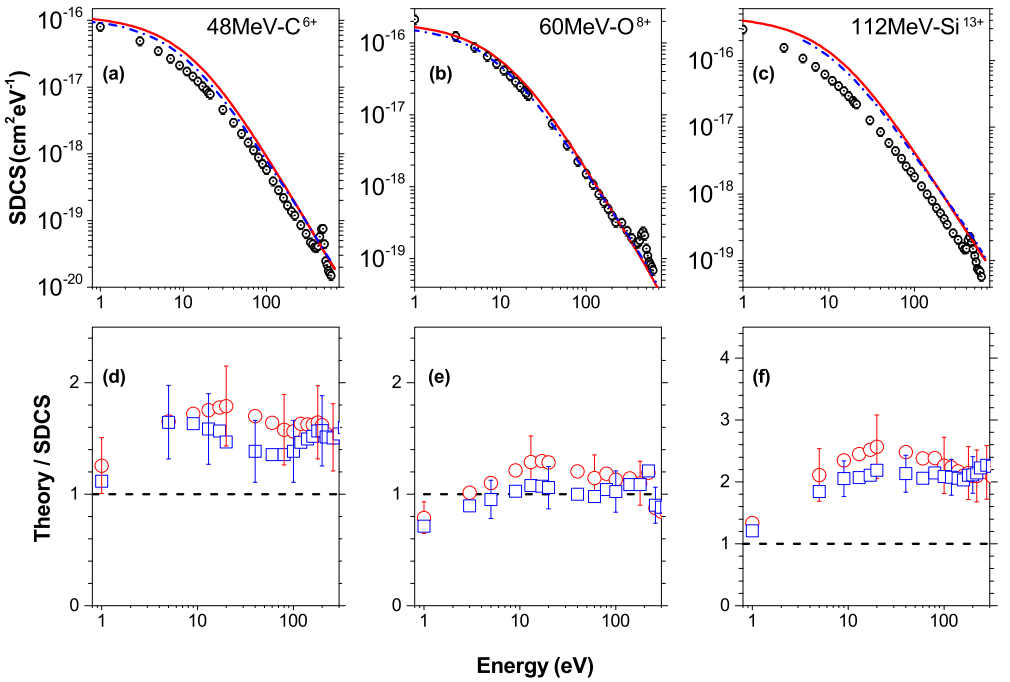

FIG. 9. Energy distribution of the absolute electron SDCS for 4-MeV/u C^{6+} (a), 3.75-MeV/u O^{8+} (b), and 4-MeV/u Si^{13+} (c). The solid (red) line corresponds to the CDW-EIS prior version and the dash-dotted (blue) line corresponds to the post-version. Plots (d)–(f) show the ratio of measured SDCS with the CDW-EIS model [both prior (circle)] and post (square)].

that the present experimental TCS values for both C^{6+} and Si^{13+} projectiles are smaller than the theoretical predictions. In the case of the C^{6+} projectile, total cross section values calculated using the prior version of the CDW-EIS model overestimates the experimental data by ≈70%, while the post-version overestimates the data by ≈50%. For the Si^{13+} projectile the CDW-EIS prior model overestimates the data by ≈130% while the post-version overestimates the data by ≈85%. The TCS for the 72-MeV O^{8+} projectile is a revised value obtained from our earlier publication [29,43].

1. Scaled total cross section

The ionization processes in a collision event depend on the perturbation strength ($\frac{q_p}{v_p}$) of the projectile. Here q_p and v_p denote the projectile charge state and velocity, respectively.

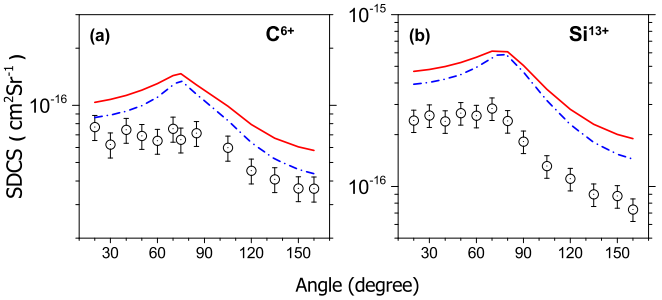

FIG. 10. Angular distribution of the absolute electron SDCS for two different projectile beams, 4-MeV/u C^{6+} (a) and 4-MeV/u Si^{13+} (b). In each plot, the solid (red) line corresponds to the CDW-EIS prior version calculation while the dash-dotted (blue) line corresponds to the post-version.

A quadratic q_p dependence of the single ionization cross section (σ_{tot}) of atoms in fast collisions is well known from the experiments and is well predicted by the first-order perturbative models. It can be seen from the DDCS spectra that one of the main contributions to the TCS values should come from the soft collision process. In Fig. 11(a), we have shown the velocity dependence of σ_{tot}/q_p^2 for the water molecule under the impact of five different projectiles, namely, H^+ (taken from [17,22,44]), He^{2+} (taken from [25,45]), C^{6+} (taken from [27]), O^{8+} [29,30,42], and C^{6+} and Si^{13+} data (taken from the present study). For light projectiles H^+ and He^{2+}, the scaled total cross section (σ_{tot}/q_p^2) results fall on a line representing the q_p^2 dependence. However, our present data with heavier ions, clearly fall below the line, indicating a gradually increasing deviation from q_p^2 dependence. It seems that $\sigma_{tot} \sim q_p^n$ where n is less than 2. The value of n depends upon the projectile. Interestingly a similar kind of behavior for the 6-MeV/u C^{6+} projectile was observed by Ohsawa *et al.* [27]. Their measured TCS data also fall below the Bethe-Born predicted line [46,47]. These two data points for C^{6+} ions (existing data at 6 MeV/u [27] and our present

TABLE III. Total ionization cross section in units of 10^3 Mb.

Projectile	Expt.	CDW-EIS (prior)	CDW-EIS (post)
48-MeV C^{6+}	0.72	1.25	1.06
48-MeV O^{8+}	2.33 [30]	2.8	2.5
60-MeV O^{8+}	2.03 [42]	2.4	2.1
72-MeV O^{8+}	1.45* [29]	2.1	1.8
112-MeV Si^{13+}	2.31	5.09	4.33

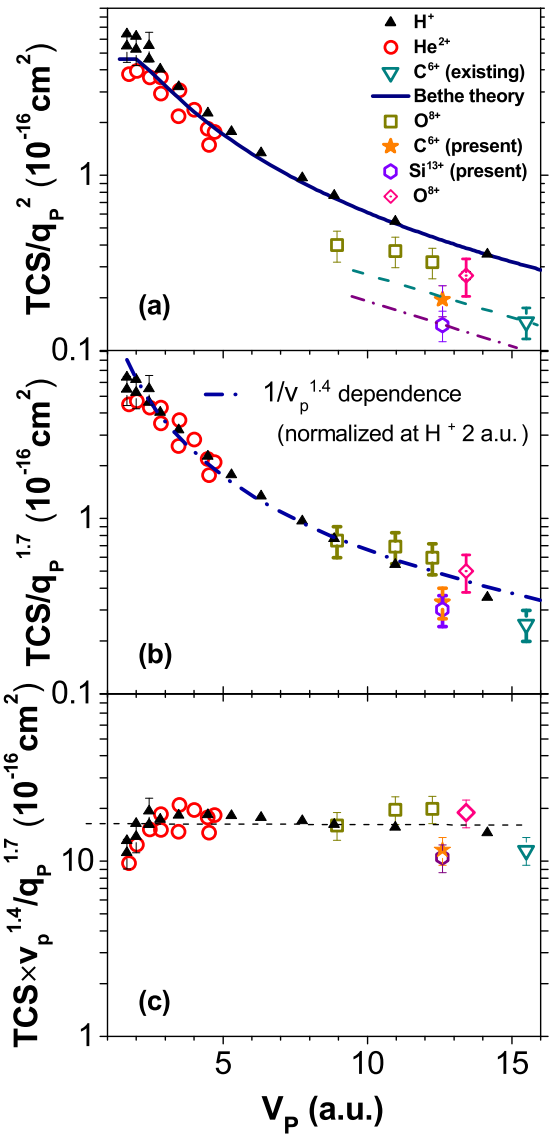

FIG. 11. The projectile velocity dependence of TCS/q_p^2 (a), TCS/$q_p^{1.7}$ (b), and TCS $\times$ $v_p^{1.4}/q_p^{1.7}$ (c) for H_2O under the impact of different projectiles. The H^+ data (solid up-triangle) are taken from [17,22,44], He^{2+} data (circle) from [25,45], C^{6+} data (open down-triangle) taken from [27], and C^{6+} (star) and Si^{13+} (hexagon) data the present study. The three data points (square) for O^{8+} represent our previous experiment with the O^{8+} beam on the water vapor target, while the fourth O^{8+} data point (diamond) is taken from [29].

data at 4 MeV/u) joined by a line (dashed) goes parallel to the Bethe-Born predicted line. The scaled TCS data for O (□) again falls below the Bethe line. But O data show less deviation from the expected line compared to C^{6+} data. Because of the mismatch in scaled cross section data for highly charged projectiles, all the TCS values were scaled again. Figure 11(b) represents the plot for that, where we have plotted the velocity dependence of $\sigma_{tot}/q_p^{1.7}$ for the same projectiles. It can be seen that the scaled cross-section data for almost all the projectiles fall on a band. We can therefore infer that TCS $\sim$ q_p^n where $n \approx 1.7 \pm 0.1$. It can be mentioned that in a previous work with the uracil target and highly charged oxygen, carbon, fluorine projectiles [5], n was found to be $\approx$1.5. A possible reason for the smaller value of n for the case of uracil may be because of its larger size compared to the water molecule, thus giving rise to a larger deviation from the q_p^2 dependence. In Fig. 11(c) we have plotted the fully scaled TCS, i.e., $\sigma_{tot} \times v_p^{1.4}/q_p^{1.7}$ as a function of projectile velocity. From the figure it is clear that for projectile velocity greater than about 2 a.u., the data points (fully scaled) fall on a horizontal line, i.e., a constant of value 16 $\times 10^{-16}$ ($\pm$20%) indicating a $1/v_p^{1.4}$ dependence of the TCS. The data points for $v_p \leqslant 2$ a.u. show a fall indicating the deviation from the scaling behavior at this low velocity for which v_p approaches the electron orbital velocity. At this velocity TCS shows a broad peaking behavior. Therefore, we can predict, for the water molecule, TCS$= 16 \times q_p^{1.7}/v_p^{1.4} \times 10^{-16}$ cm^2, if $v_p \geqslant 2$ a.u. But, in any case, it may be emphasized that this scaling law can only give orders of magnitude since significant deviations are observed for the highly charged projectiles (HCI) [see Figs. 11(b) and 11(c)]. Such deviation is not unexpected since for HCIs the perturbation strength q_p/v_p is relatively large and therefore the simple scaling based on first-order perturbative models may not be valid. One may expect higher order terms (such as in the Born series) need to be included in any modeling.

V. CONCLUSIONS

We have investigated the electron DDCS spectrum arising in ionization of water molecules under the impact of 4-MeV/u C^{6+} and Si^{13+} projectile ions. The obtained data include the DDCS spectrum for the energy range of 1–600 eV and angular range of 20°–160°. Occasionally the previous data for similar velocity (3.75-MeV/u) O^{8+} projectile, have been used for the sake of comparison with the present set of data. The obtained data were compared with both the prior and post-versions of the CDW-EIS model. The current data exhibit a reasonable agreement with theoretically calculated values for the case of C^{6+} and O^{8+} projectiles. Out of all the three projectiles the O^{8+} shows best agreement with the theoretical models. Quite unexpectedly, the deviations from the theoretical predictions are larger for C ions than for O ions. Further measurements are needed to clarify this discrepancy. Maximum deviation from theoretical predictions can be seen for the Si^{13+} projectile. A possible explanation of the overall overestimation of experimental data could be that, as the projectile charge increases, the excitation of the target could play an important role coupling with ionization. This influence is not considered in the present theoretical model. Also for all the projectiles, the mismatch between theory and experimental results is maximum for the angles between 75° and 105°. Finally we observed a clear deviation from the first-order model predicted q_p^2/v_p^2 dependence of the TCS. Our all measured TCS data, along with other available data predict that the TCS varies as $\sim q_p^{1.7}/v_p^{1.4}$. The scaling constant is found to be 16×10^{-16}cm^2 ($\pm$20%) for ion-induced ionization of the water molecule for projectile velocity $\geqslant$2 a.u.

[1] B. Boudaiffa, P. Cloutier, D. Hunting, M. A. Huels, and L. Sanche, Science **287**, 1658 (2000).

[2] D. Schardt, T. Elsässer, and D. Schulz-Ertner, Rev. Mod. Phys. **82**, 383 (2010).

[3] A. N. Agnihotri, S. Kasthurirangan, S. Nandi, A. Kumar, M. E. Galassi, R. D. Rivarola, O. Fojón, C. Champion, J. Hanssen, H. Lekadir *et al.*, Phys. Rev. A **85**, 032711 (2012).
[4] A. N. Agnihotri, S. Nandi, S. Kasthurirangan, A. Kumar, M. E. Galassi, R. D. Rivarola, C. Champion, and L. C. Tribedi, Phys. Rev. A **87**, 032716 (2013).
[5] A. N. Agnihotri, S. Kasthurirangan, S. Nandi, A. Kumar, C. Champion, H. Lekadir, J. Hanssen, P. F. Weck, M. E. Galassi, R. D. Rivarola *et al.*, J. Phys. B **46**, 185201 (2013).
[6] P. Moretto-Capelle and A. Le Padellec, Phys. Rev. A **74**, 062705 (2006).
[7] J. Tabet, S. Eden, S. Feil, H. Abdoul-Carime, B. Farizon, M. Farizon, S. Ouaskit, and T. D. Märk, Phys. Rev. A **82**, 022703 (2010).
[8] Y. Iriki, Y. Kikuchi, M. Imai, and A. Itoh, Phys. Rev. A **84**, 032704 (2011).
[9] Y. Iriki, Y. Kikuchi, M. Imai, and A. Itoh, Phys. Rev. A **84**, 052719 (2011).
[10] A. Itoh, Y. Iriki, M. Imai, C. Champion, and R. D. Rivarola, Phys. Rev. A **88**, 052711 (2013).
[11] J. Schutten, F. J. De Heer, H. R. Moustafa, A. J. H. Boerboom, and J. Kistemaker, J. Chem. Phys. **44**, 3924 (1966).
[12] T. D. Märk and F. Egger, Int. J. Mass Spectrom. Ion Phys. **20**, 89 (1976).
[13] M. Murakami, T. Kirchner, M. Horbatsch, and H. J. Lüdde, Phys. Rev. A **85**, 052713 (2012).
[14] F. Alvarado, R. Hoekstra, and T. Schlathölter, J. Phys. B **38**, 4085 (2005).
[15] U. Werner, K. Beckord, J. Becker, and H. O. Lutz, Phys. Rev. Lett. **74**, 1962 (1995).
[16] F. Gobet, S. Eden, B. Coupier, J. Tabet, B. Farizon, M. Farizon, M. J. Gaillard, M. Carré, S. Ouaskit, T. D. Märk *et al.*, Phys. Rev. A **70**, 062716 (2004).
[17] M. E. Rudd, T. V. Goffe, R. D. DuBois, and L. H. Toburen, Phys. Rev. A **31**, 492 (1985).
[18] U. Bechthold, J. Ullrich, U. Ramm, G. Kraft, S. Hagmann, D. R. Schultz, C. O. Reinhold, and H. Schmidt-Böcking, Phys. Rev. A **58**, 1971 (1998).
[19] Z. D. Pešić, J.-Y. Chesnel, R. Hellhammer, B. Sulik, and N. Stolterfoht, J. Phys. B **37**, 1405 (2004).
[20] P. Sobocinski, Z. D. Pešić, R. Hellhammer, D. Klein, B. Sulik, J.-Y. Chesnel, and N. Stolterfoht, J. Phys. B **39**, 927 (2006).
[21] H. Luna and E. C. Montenegro, Phys. Rev. Lett. **94**, 043201 (2005).
[22] M. A. Bolorizadeh and M. E. Rudd, Phys. Rev. A **33**, 882 (1986).
[23] L. H. Toburen and W. E. Wilson, J. Chem. Phys. **66**, 5202 (1977).
[24] M. A. Bolorizadeh and M. E. Rudd, Phys. Rev. A **33**, 888 (1986).
[25] L. H. Toburen, W. E. Wilson, and R. J. Popowich, Radiat. Res. **82**, 27 (1980).
[26] D. Ohsawa, Y. Sato, Y. Okada, V. P. Shevelko, and F. Soga, Phys. Rev. A **72**, 062710 (2005).
[27] C. Dal Cappello, C. Champion, O. Boudrioua, H. Lekadir, Y. Sato, and D. Ohsawa, Nucl. Instr. Meth. Phys. Res. B. **267**, 781 (2009).
[28] D. Ohsawa, H. Tawara, F. Soga, M. E. Galassi, and R. D. Rivarola, Phys. Scr. **2013**, 014039 (2013).
[29] S. Nandi, S. Biswas, A. Khan, J. M. Monti, C. A. Tachino, R. D. Rivarola, D. Misra, and L. C. Tribedi, Phys. Rev. A **87**, 052710 (2013).
[30] S. Bhattacharjee, S. Biswas, C. Bagdia, M. Roychowdhury, S. Nandi, D. Misra, J. M. Monti, C. A. Tachino, R. D. Rivarola, C. Champion *et al.*, J. Phys. B **49**, 065202 (2016).
[31] D. Ohsawa, H. Tawara, F. Soga, M. E. Galassi, and R. D. Rivarola, in *Journal of Physics: Conference Series* (IOP Publishing, Bristol, 2014), Vol. 488, p. 102030.
[32] P. D. Fainstein, G. H. Olivera, and R. D. Rivarola, Nucl. Instr. Meth. Phys. Res. B. **107**, 19 (1996).
[33] C. A. Tachino, J. M. Monti, O. A. Fojón, C. Champion, and R. D. Rivarola, J. Phys. B **47**, 035203 (2014).
[34] D. S. F. Crothers and J. F. McCann, J. Phys. B **16**, 3229 (1983).
[35] P. D. Fainstein, V. H. Ponce, and R. D. Rivarola, J. Phys. B **21**, 287 (1988).
[36] B. Senger and R. V. Rechenmann, Nucl. Instr. Meth. Phys. Res. B **2**, 204 (1984).
[37] B. Senger, Z. Phys. D **9**, 79 (1988).
[38] E. Clementi and C. Roetti, At. Data Nucl. Data Tables **14**, 177 (1974).
[39] R. Moccia, J. Chem. Phys. **40**, 2164 (1964).
[40] D. Misra, K. V. Thulasiram, W. Fernandes, A. H. Kelkar, U. Kadhane, A. Kumar, Y. Singh, L. Gulyas, and L. C. Tribedi, Nucl. Instr. Meth. Phys. Res. B. **267**, 157 (2009).
[41] P. D. Fainstein, L. Gulyás, F. Martin, and A. Salin, Phys. Rev. A **53**, 3243 (1996).
[42] S. Bhattacharjee, C. Bagdia, M. Roy Chowdhury, J. M. Monti, R. D. Rivarola, and L. C. Tribedi, Eur. Phys. J. D (to be published) (2017).
[43] The earlier experiment with 72-MeV O^{8+} on water vapor (originally published in Ref. [29]) was repeated later for a few more energies [Ref. [30]] with a much improved background-to-data ratio which was achieved by keeping the chamber warm, as has been done in the present experiment. This was explained in our last paper on water [30]. We found that the data taken with much reduced water-background provided TCS which was about 33% lower than that obtained without heating the chamber. Therefore, the earlier TCS data in Ref. [29] need to be revised and these modified TCS data have now been shown in Figs. 10(a) and 10(b). The revised data are 33% less than the original data.
[44] M. E. Rudd, Y.-K. Kim, D. H. Madison, and T. J. Gay, Rev. Mod. Phys. **64**, 441 (1992).
[45] M. E. Rudd, T. V. Goffe, and A. Itoh, Phys. Rev. A **32**, 2128 (1985).
[46] M. Inokuti, Rev. Mod. Phys. **43**, 297 (1971).
[47] M. Inokuti and M. McDowell, J. Phys. B **7**, 2382 (1974).